Softening, Hardening, and Precipitation Evolution of the AA6082-T651 Heat-Affected Zone Caused by Thermal Cycles During and After Welding

Mohammad Jula[1] · Reza Dehmolaei[1] · Khalil Ranjbar[1]

Abstract

In this study, gas tungsten arc welding (GTAW) was used to weld AA6082-T651 plates using ER5335 and ER4340 filler metals. Significant softening of the heat-affected zone (HAZ) was observed in the as-welded condition. An attempt was made to recover the softening by applying an appropriate heat treatment after welding. The thermal process consisted of solution annealing and then aging at 160 °C for 18 h. The HAZ properties were characterized in the as-welded and post-weld heat-treated (PWHT) conditions using field emission scanning and high-resolution transmission electron microscopy, microhardness testing, thermal simulation, and differential scanning calorimetry techniques. The HAZ hardness profile revealed four distinct regions: partially melted zone (PMZ), partial solution, over-aged zone, and partial transformation. A PMZ with a hardness of about 90 Vickers was detected adjacent to the fusion line, which had been exposed to a sufficient temperature to dissolve the Mg_2Si phases completely. Accordingly, natural aging increased the hardness of PMZ after welding. The minimum HAZ hardness was found at a distance of about 7–9 mm from the fusion line, where the temperature was in the range of β-Mg_2Si formation and resulted in over-aging. In addition, dislocation density was reduced compared to the as-received base metal. The hardness after PWHT exhibited full recovery and improved to values higher than the as-received base metal. The hardness recovery was attributed to the uniformly distributed fine coherent needle-shaped β''-Mg_2Si after PWHT. There were also coarse $Al_{15}(Fe,Mn)_3Si_2$ intermetallic and submicron spherical Mn-rich dispersoids in all conditions.

Keywords 6082 aluminum alloy · Welding thermal cycles · Heat-affected zone · Post-weld heat treatment · Hardness recovery · Precipitate evolution

1 Introduction

The 6082 alloy belongs to the 6000 series aluminum alloy with Mg and Si as the main alloying elements. This alloy is precipitation hardened via solution annealing and aging treatment, where yield strength can be increased to about 300 MPa [1, 2]. This aluminum alloy possesses desirable properties, including a high strength-to-weight ratio, excellent workability, and superior corrosion resistance. The 6082 alloy is widely used in various structural applications [3, 4], particularly in the automobile industry and shipbuilding [5, 6].

As a widely used industrial material, fusion welding is the most common joining technique for this alloy. Nevertheless, fusion welding encounters some challenges. The welding of these alloys is sensitive to weld metal hot cracking, especially when the welding is performed with similar or no filler metal [7, 8]. Welding heat input causes precipitate evolution, including precipitate dissolution, growth, and transformation, in different weld zones, particularly in the HAZ [9–11], and extends the HAZ, typically between 10 and 30 mm from the fusion line [11, 12]. Generally, it is accepted that in 6000 series aluminum alloys, the HAZ is the weakest region, and the HAZ exhibits lower strength and hardness than the base metal. It is attributed to the softening effect that leads to a remarkable reduction of the proof strength and hardness in the HAZ. Previous studies [13, 14] reported that the weld joint strength in 6xxx alloys may decrease to half its initial

✉ Reza Dehmolaei
Dehmolaei@scu.ac.ir

1 Department of Materials Science and Engineering, Faculty of Engineering, Shahid Chamran University of Ahvaz, Ahvaz, Iran

value in the T-6 condition. In other words, the extent of strengthening and softening is strongly controlled via precipitate evolution.

In a typical heat treatment (artificial aging), the general sequence of precipitate evolution for the Al-Mg-Si alloy includes the following [15, 16]:

SSSS_GP zones_β∗∗-Mg2Si_β∗-Mg2Si_β-Mg2Si

The unstable supersaturated solid solution (SSSS) may follow the above sequence depending upon the aging conditions. Each precipitate has its size, distribution, coherency, thermal stability, and morphology, which significantly influence the strengthening of the matrix. It is reported that only coherent GP zones are formed during natural aging, and strengthening is not maximized due to the absence of other strengthening precipitates [6, 17, 18]. In artificial aging, the most strengthening effect is induced by the coherent elongated β''-Mg_2Si phase. Subsequently, the coarse and rod-shaped β'-Mg_2Si phase is formed in an over-aged condition. In this sequence, at last, the β-Mg_2Si is formed, which is an equilibrium phase. Similar to β'-Mg_2Si, the β-Mg_2Si phase also reduces the maximum strength [19, 20].

Therefore, in any thermal cycle like fusion welding, it is crucial to characterize and control the precipitate type to obtain appropriate properties and prevent softening. In this regard, Missori et al. [21] studied the mechanical properties of the weld metal in 6082-T6 alloy and reported the lowest hardness value in the HAZ at a 6 mm distance from the Fusion line. They also found a 60% reduction in the weld metal strength due to over-aging. Baskutis et al. [22] investigated the effect of different welding parameters on the mechanical properties of weld in the 6082 -T6 alloy system. They noticed a PMZ at the welding interface with the highest hardness of 92 VHN and HAZ softening due to precipitate coarsening and over-aging. For the same alloy system, Zhang et al. [23] studied the effect of the paint-baking treatment on the mechanical properties of the HAZ, but the applied treatment could not completely recover the hardness and strength of the HAZ. Similarly, Wang et al. [24] investigated HAZ softening of the same alloy, considering the effect of welding heat input and post-weld heat treatment. It was demonstrated that in all the solution annealed and aged samples, fracture occurred in the weld only, whereas, under low and high heat input, fracture occurred in the weld and the HAZ, respectively. Previous studies [23–25] suggested post-weld heat treatment to recover the softening, but the attempts were not entirely successful.

Therefore, based on the literature review, it can be noted that HAZ is severely susceptible to softening during fusion welding. While considering the problem, in this study, 6082 aluminum alloy was welded by the gas tungsten arc welding (GTAW) process, and an appropriate post-weld heat treatment was adopted. The purpose of the applied heat treatment was to completely recover the hardness and form the desired β''-Mg_2Si phases in the HAZ.

2 Materials and methods

In the present research, the commercial grade rolled 6082-T651 plates with 6 mm thickness were used as the base metal. First, samples with dimensions of $200 \times 75 \times 6$ mm were cut from the base metal. As shown in Fig. 1, all butt joints were assembled in a machined 70° V-groove without a root gap. ER4043 and ER5356 filler metals with a diameter of 2.4 mm were used. The chemical composition of the base and filler metals is given in Table 1. In the GTAW process, an un-consumable zirconated tungsten electrode with a diameter of 3.2 mm was used. Welding was performed using the GTAW process with an alternative current (square wave). Argon gas, with a purity of 99.99%, was used to shield the weld zone. The shielding and purging gas flow rates were 14 and 10 lit/min, respectively. The welding parameters are presented in Table 2. Welding was done in such a way that initially, a backing weld was deposited on the root side, and then a cap (filling) pass filled the groove from the opposite side. Figure 1 shows a schematic view of the joint design adopted in the present study.

A thermal simulation of the welding process was performed to assess the thermal cycle in the HAZ. For this purpose, Solid works and Hyper mesh software were adopted for the geometric design and meshing. For the thermal simulation, Simufact welding was used. Three K-type thermocouples were implanted in every welding pass to calibrate the input data and verify the output results obtained from the software. A schematic view of the weld geometry and the meshing condition is illustrated in Fig. 2. Thermal analysis was performed to determine the temperature distribution using Eq. 1. In this research, the thermal distribution of double ellipsoids provided by Goldak has been used to model the heat source of the welding process. Equations 2 and 3
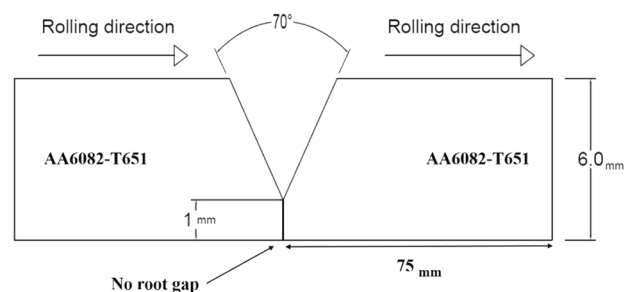

Fig. 1 Schematic view of the weld joint

Table 1 Chemical composition of as-received base metal and filler metals (Wt %)

	Si	Mg	Mn	Fe	Cu	Cr	Ti	Zn	Al
AA6082	0.90	0.78	0.57	0.31	0.03	0.03	0.003	0.04	Base
ER4043 *	4.5-6.0	0.05	0.05	0.8	0.30	–	0.20	0.010	Base
ER5356 *	0.25	4.5–5.5	0.05–0.20	0.40	0.10	0.05–0.20	0.06–0.20	0.10	Base

*For ER4043 and ER5356, the single values are maximum

Table 2 Welding parameters

Sample no.	Type of filler metal	Pass	Frequency (Hz)	Duty cycle (%)	Current (A)	Voltage (V)	Time (S)
1	ER4043	Backing weld	50	50	190	18	69
		Cap	50	50	190	18	126
2	ER5356	Backing weld	50	50	190	18	78
		Cap	50	50	190	18	104

Table 3 Geometric characteristics of the molten pool based on Goldak's model for a heat source

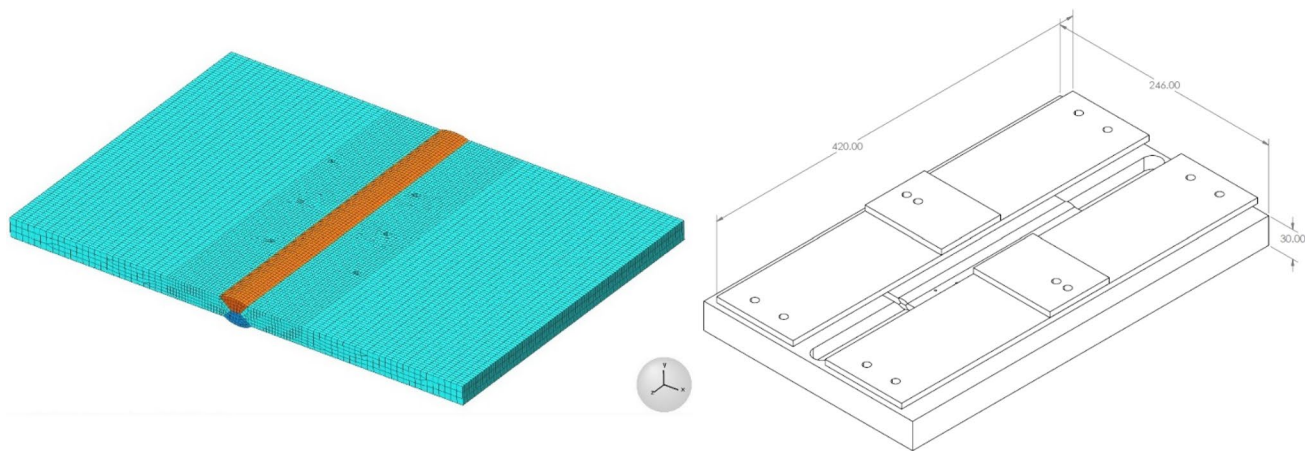|		Pass	Front length (c_f), mm	Rear length (c_r), mm	Depth (a), mm	Half width (b), mm
1	ER4043	Backing weld	1.2	1.3	3.9	4.6
		Cap	1.3	1.5	4.5	5.3
2	ER5356	Backing weld	1.2	1.3	4.1	4.7
		Cap	1.3	1.4	4.3	5.1

Fig. 2 Geometry and meshing condition of welded samples

are related to Goldak's model. The geometric characteristics of Goldak's model are listed in Table 3.

$$k\left(\frac{\partial^2 T}{\partial x^2}\right) + k\left(\frac{\partial^2 T}{\partial y^2}\right) + k\left(\frac{\partial^2 T}{\partial z^2}\right) + G = \rho C \frac{\partial T}{\partial t} \quad (1)$$

where k, T, G, ρ, and C are specific thermal conductivity, temperature, internal heat source, material density, and specific heat capacity, respectively.

$$\begin{cases} q_f = \frac{6\sqrt{3}f_f q}{abc_f \pi \sqrt{\pi}} \exp\left[-3\left(\frac{y}{b}\right)^2 - 3\left(\frac{z}{a}\right)^2 - \left(\frac{x}{c_f}\right)^2\right] \forall x \geq 0 \\ q_r = \frac{6\sqrt{3}f_r q}{abc_r \pi \sqrt{\pi}} \exp\left[-3\left(\frac{y}{b}\right)^2 - 3\left(\frac{z}{a}\right)^2 - \left(\frac{x}{c_r}\right)^2\right] \forall x \leq 0 \end{cases} \quad (2)$$

where q is the power input, and a, b, c_f, and c_r are the geometrical characteristics of the heat source; f_f and f_r are fractions of heat deposited in the front and rear quadrants,

respectively. In addition, the following criteria ensure the continuity of the heat source.

$$\begin{cases} \frac{f_f}{c_f} = \frac{f_r}{c_r} \\ f_f + f_r = 2 \end{cases} \tag{3}$$

After welding, the welded plates were cut perpendicular to the welding line and parted into two halves. One half was stored at room temperature in as-welded condition for four weeks, and the other part was subjected to a PWHT. In the latter case, heat treatment was composed of solution annealing for two hours, quenching in water, and instant aging at 160 °C for 18 h.

Vickers microhardness tests were carried out across the weld cross-section with a 200 g load at a 10 s dwell-time according to the ASTM E 384-99 standard [26].

Micrographic analysis was carried out using a scanning electron microscope (SEM) Model: MIRA3-TESCAN equipped with an energy dispersive x-ray spectroscopy (EDX). Specimens for transmission electron microscopy (TEM) analysis were prepared according to the standard metallographic procedure. Microstructural features, including precipitate type and morphology at the cross-section of the welded joints, were examined by TEM and high-resolution transmission electron microscopy (HRTEM). Specimens were initially sliced perpendicular to the seam to about 2 mm in thickness by wire cut electrical discharge machining from the HAZ in the as-welded and post-weld conditions. The location of the TEM specimen corresponds to a distance of 7 mm from the weld fusion line, where a minimum hardness was obtained. Then, TEM specimens were mechanically ground to about 100 μm and further thinned by twin-jet electropolishing. TEM observations were performed on an FEI HR(S)TEM system (model: Tecnai G^2 F20 S-TWIN, USA), operated at 200 kV.

Diffraction scanning calorimetry (DSC) was used to determine the phase transformation temperature range. DSC specimen was taken from as-received base metal. The test was carried out in the range of 25–530 °C for as-received AA6082-T651 with a 10 K/min heating rate.

3 Results and Discussion

This section presents the research results, analysis, and discussion of the data. The section is developed in three general parts: AA6082-T651 base metal, HAZ in as-welded conditions, and HAZ after PWHT. In the first part, the microstructure and mechanical properties of the base metal are studied. Then in the second part, the changes in mechanical properties and microstructure after welding are evaluated. Finally, the effect of PWHT on HAZ properties is explained.

3.1 AA6082-T651 base Metal

This sub-section presents the microstructure and mechanical properties of the as-received AA6082-T651 base metal. A scanning electron microscopy image (Fig. 3) shows the presence of bright phases (higher density) with different dimensions and morphologies in the α-aluminum matrix. The results of the EDS analysis (Table 4) revealed that high-density secondary phases are rich in iron, manganese, and silicon. The figure shows that the α-Al$_{15}$(Fe,Mn)$_3$Si$_2$ phases with both Chinese script (B, D, and F) and blocky (C and E) morphologies are formed, while the harmful phases, such as the needle-like β-Al$_9$Fe$_2$Si$_2$, are not observed. Indeed the presence of manganese in the secondary phases has prevented the formation of harmful needle-like β-Al$_9$Fe$_2$Si$_2$ and encouraged the formation of α-Al$_{15}$(Fe,Mn)$_3$Si$_2$ with different morphologies. Previous researchers have reported similar results on the effect of Mn on Al-Fe-Si intermetallic modification [27–29].

The results of the transmission electron microscope (Fig. 4) have shown the microstructure at the sub-micron scale. According to the references [30, 31] and the single-phase aluminum FCC SAED pattern, the dark lines in Fig. 4a relate to the dislocations. Given that the base metal has been wrought (rolled), the density of dislocations has increased due to cold work. The lattice strength relates to the square root of the dislocation density, so increasing the dislocation density increases the material's strength. In contrast to the previous case, the SAED pattern in Fig. 4b shows the presence of a secondary phase in addition to the α-aluminum FCC matrix. The SAD spots of the Al matrix are indexed in Fig. 4b, and the other weaker spots are related to precipitate. Due to the darkness of this phase in the bright field image, its density is higher than the aluminum matrix. According to the EDS results (Fig. 4c), this phase is rich in manganese and has lower iron, silicon, and copper in its chemical composition. These fine and dispersed precipitates can increase hardness and strength. Nam and Lee [32] have investigated the effect of Mn on the mechanical behavior of Al alloys. They reported that the formation of fine Mn-containing dispersoids leads to higher as-extruded yield strength because dispersoids retard the dislocation motion and prevent dislocation cross-slip. Other researchers have also reported improved mechanical properties due to Mn-containing dispersoids [33, 34]. Muggerud et al. [35, 36] have reported that the fine Mn-containing dispersoids are Al$_6$(Mn,Fe) or α-Al(Mn,Fe)Si. If Si is sufficient, the presence of α-Al(Mn,Fe)Si phase is more probable. They concluded that the orientation relationship between α-Al(Mn,Fe)Si and Al matrix can be expressed as [1$\bar{1}$1]α // [1$\bar{1}$1]$_{Al}$ and (5$2\bar{7}$)α // (011)$_{Al}$. Li et al. [37] have reported similar results on the orientation relationship and concluded that fine α-Al(Mn,Fe) Si dispersoids are partially coherent.
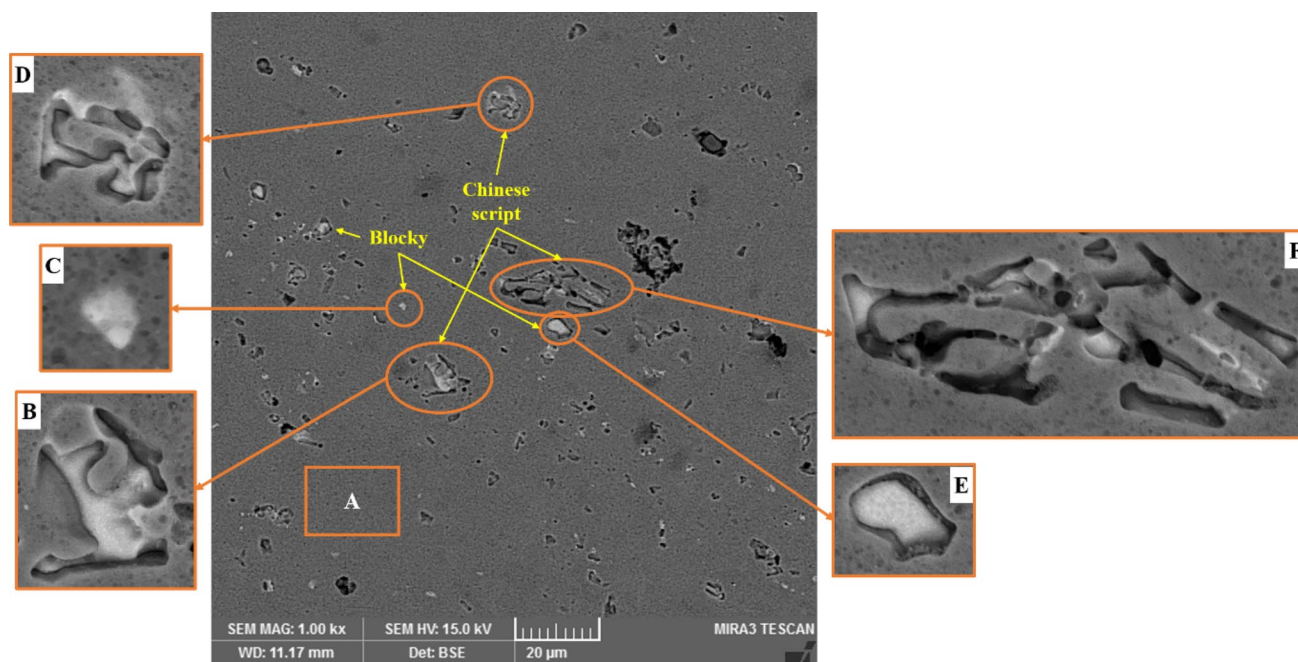
Fig. 3 Scanning electron microscope images of as-received AA6082-T651 base metal

Table 4 EDS analyses of indicated phases in Fig. 2

Element (Wt %)	Al	Si	Mg	Mn	Fe
A	96.48	2.06	1.06	0.32	0.08
B	67.22	6.97	–	9.60	16.21
C	75.06	5.51	0.66	6.35	12.43
D	73.55	3.53	0.57	7.48	14.87
E	66.61	6.10	0.41	8.81	18.07
F	66.75	7.61	0.37	8.41	16.85

The alloy designation indicates that the base metal must be age-hardened. The Mg_2Si phase in the as-received base metal microstructure is shown in Fig. 5. The aluminum matrix spots indexed in the SAD pattern and other weaker spots correspond to the indicated precipitate. According to previous research, β''-Mg_2Si needles are up to 50 nm long and about 4 nm in diameter, and β'-Mg_2Si rods are several hundreds of nm long and 10–15 nm in diameter [38, 39]. Thus, the observed phase seems to be β'-Mg_2Si according to its dimensions and morphology. Theoretically, the alloy should be aged within the temperature and time range of β''-Mg_2Si formation. On the other hand, the number and distribution of phases are not enough to achieve maximum hardness and strength. However, Table 5 shows that the alloy has sufficient hardness based on reliable standards and datasheets [40]. Therefore, some of the hardness and strength in commercial alloys are due to the increased dislocation density. Aging seems to be done economically so that hardness and strength are at the standard level.

3.2 Heat-Affected Zone (HAZ) in the as-welded Condition

This sub-section explains the microstructure and mechanical properties of HAZ in as-welded conditions. Figure 6a indicates a defect-free weld joint between the weld and the base metal. Figure 6b shows high-density secondary phases similar to the base metal in the HAZ. These phases are rich in iron, manganese, and silicon (Table 6); Hence, the indicated phases in Fig. 6b and c can be Al(Mn,Fe)Si. Due to the higher density, the precipitates are lighter than the aluminum matrix in the backscattered electron image. A comparison of Figs. 3 and 6 shows that these phases are still present in the HAZ close to the fusion line. They are primarily blocky, and large precipitates with Chinese script morphology decreased, unlike the base metal. They appear to have a preferred location at the boundaries of elongated rolled grains. This can be caused by the local melting of grain boundaries and subsequent reformation or morphological changes in eutectic phases. Thus, the first part of HAZ where the morphology of iron and manganese-rich phases has changed is a partial melting zone (PMZ). However, phases with Chinese script morphology, such as those shown in Fig. 6c, are still found in the microstructure and have not been completely eliminated.
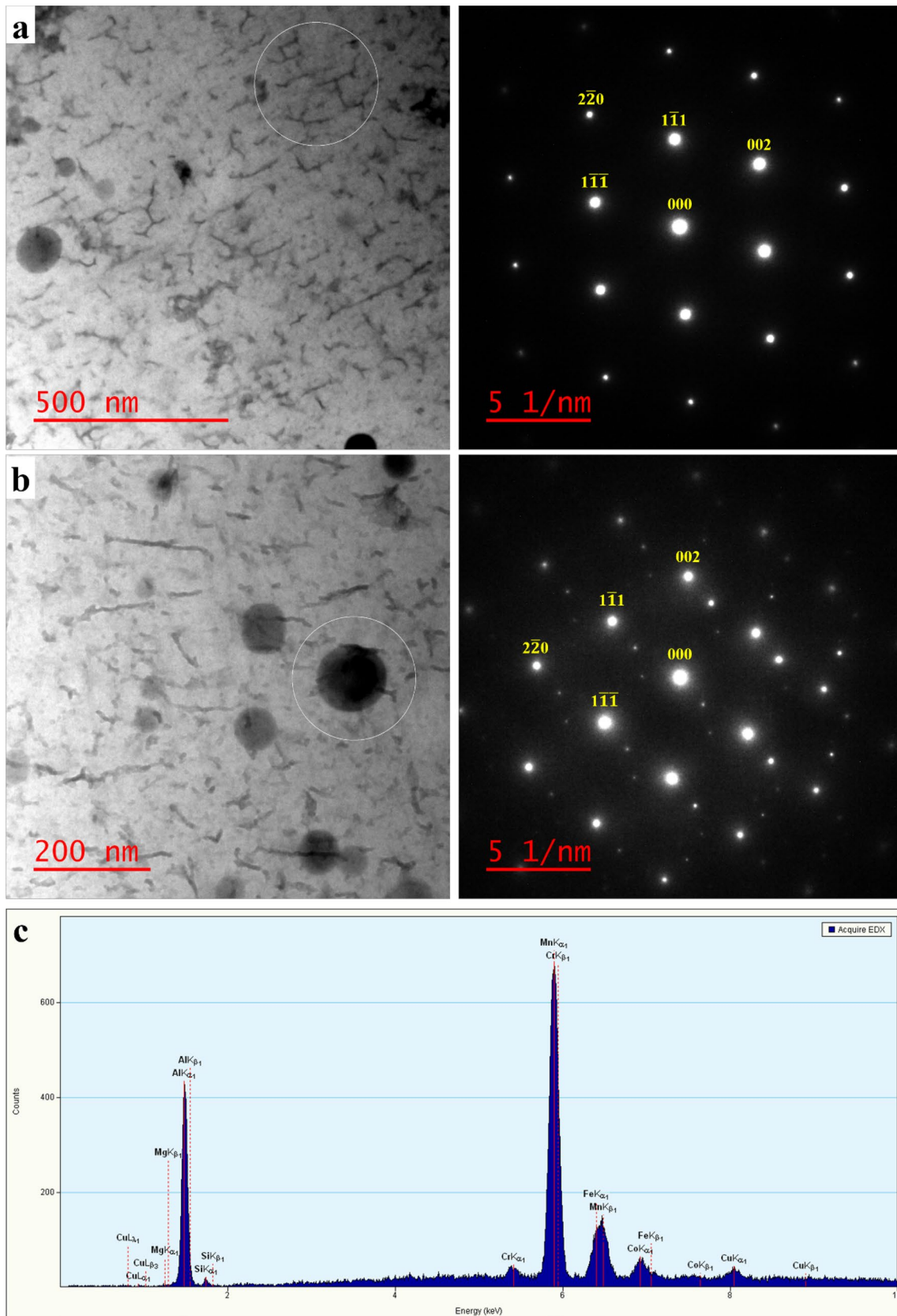
Fig. 4 TEM results of as-received AA6082-T651 base metal, **a** Microstructure with dislocations and corresponding SAD pattern, **b** high-density spherical precipitate in higher magnification and its SAD pattern, and **c** EDS analysis of the precipitate

Figure 7 represents the hardness profile from the fusion line to the unaffected base metal adjacent to both specimens' root and cap pass. Both samples have a very wide HAZ of about 24–27 mm. It is due to the high thermal conductivity of aluminum, which leads to an extensive HAZ compared to steels and nickel-based alloys. The thermal conductivity of AA6082 alloy is about 150–170 W/mK, while for AISI 316 steel and alloy 625, it is about 12.9 and 9.95 W/mK, respectively [41–43]. As a result, welding aluminum alloys requires a higher heat input despite the lower melting temperature. High heat input, similar to high thermal conductivity, leads to the extension of aluminum HAZ. In addition, a trend pattern is observed in all HAZ hardness profiles in Fig. 7, which consists of a PMZ, partial solution, over-aged zone, and partial transformation. These parts will be explained in the following.

In this paper, a thermal investigation of the HAZ was carried out with the help of thermal simulation and DSC results. Figure 8 displays the results of the thermal simulation. Figure 8a reveals the exposed peak temperature at any point of the weld cross-section, While the curves in Fig. 8b show the temperature changes of a point during welding. The results are used to study the different parts of HAZ in the following. The DSC curve in Fig. 9 shows three endothermic peaks, including a, c, and e, at temperatures of 218, 332, and 456 °C, respectively. These endothermic peaks are related to dissolution of β'', β', and β phases, which are mentioned in Fig. 9. In addition, two exothermic peaks, including b and d at 262 and 390 °C, corresponding to the formation of β'

and β are determined. Unlike the present work, Dutta et al. [44] and Miao et al. [45] reported four exothermic peaks consisting of GP zones, β'', β', and β precipitation. However, some reports have indicated that DSC results are affected by the initial conditions of the sample, such that the peaks of GP zones and β'' precipitation disappeared under the T6 conditions [46–48].

Considering all the hardness profiles in Fig. 7, it is clear that the region adjacent to the fusion line (PMZ) has a hardness of about 85–90 Vickers, which steeply declines with increasing distance from the fusion line. The thermal simulation results (Fig. 8) show that the temperature decreased from about 640–550 °C at a distance of 70–400 μm from the fusion line. The solidification range of the AA6082 is 550–650 °C [49, 50]. Therefore, the simulation results confirm the presence of a partially melted metal in this region during welding. The DSC results (Fig. 9) indicate that the base metal precipitate's solution temperature is 456 °C (peak e-solution). As a result, the temperature range of PMZ is sufficient to dissolve the Mg_2Si phases. Accordingly, the reason for the higher hardness of PMZ is the high temperature of this zone in the high ranges of solution annealing, which has rapid dissolution. The short time of the welding

Table 5 Vickers hardness test results of as-received AA6082-T651

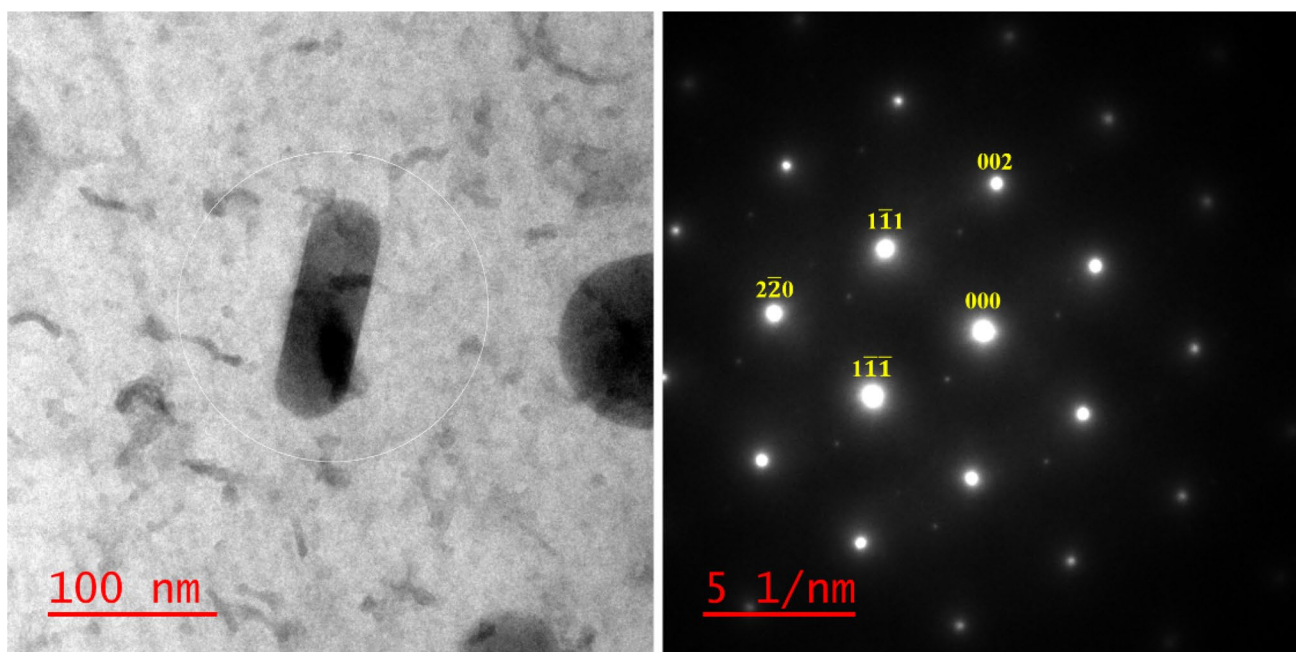| Trial 1	Trial 2	Trial 3	Mean
112.15	112.17	111.0	111.8

Fig. 5 Bright-field TEM image of the β'-Mg_2Si elongated precipitate and corresponding SAD pattern
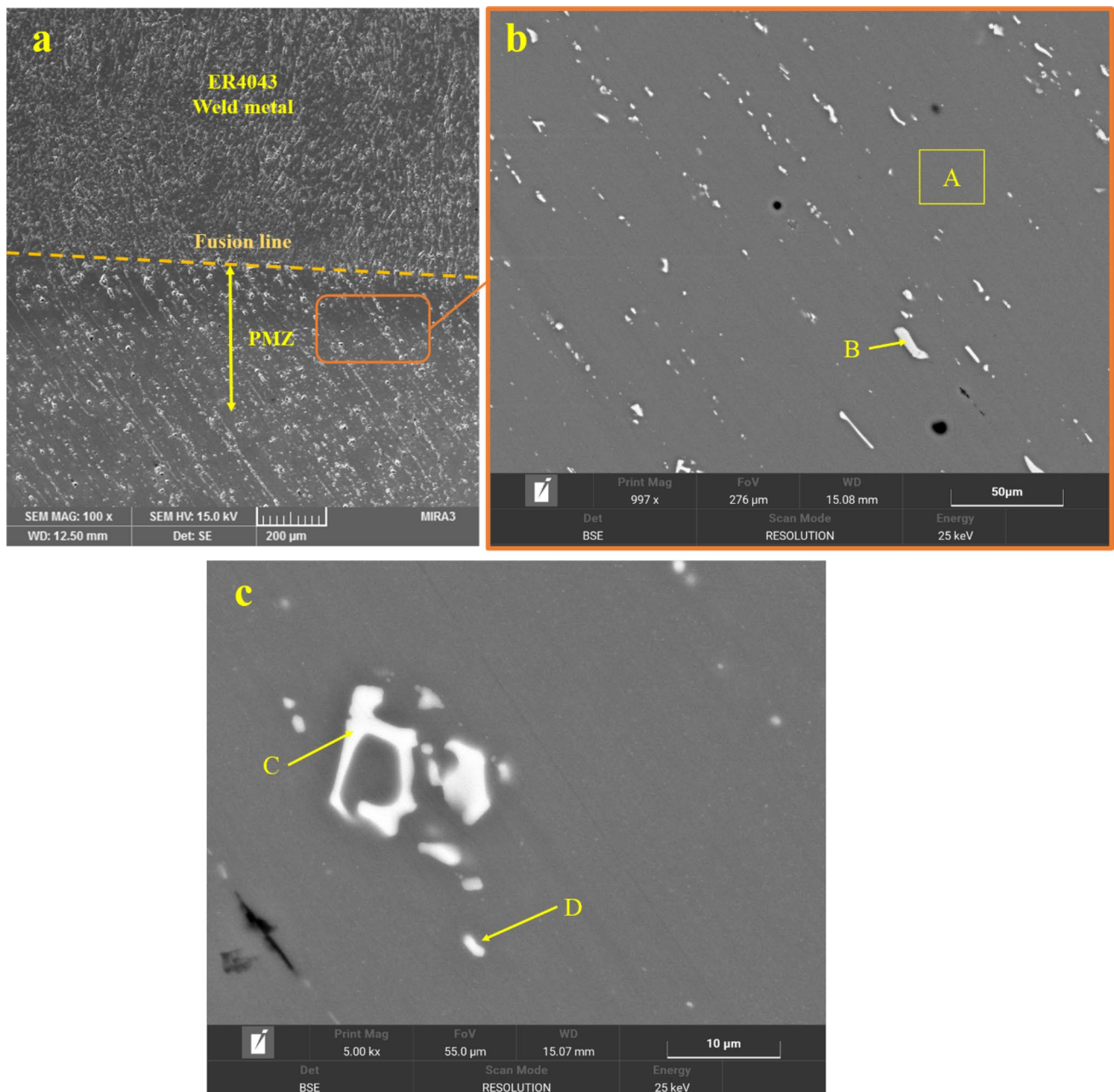
Fig. 6 Scanning electron microscope images of the HAZ adjacent to the fusion line of sample 1, **a** general view of the fusion line and PMZ, **b** distribution of secondary phases in a rolling direction, **c** a precipitate with Chinese script morphology

Table 6 EDS analyses of indicated phases in Fig. 6

Element (Wt%)	Al	Si	Mg	Mn	Fe
A	97.56	0.58	1.29	0.34	0.22
B	68.74	6.27	0.87	9.70	14.41
C	68.89	6.36	0.86	9.37	14.51
D	82.62	4.48	1.16	5.55	6.19

thermal cycle is sufficient for the complete dissolution of Mg_2Si phases. After welding, when the joint is at ambient temperature, the natural aging process increases the hardness of this area.

At a short distance from the fusion line and outside the PMZ (part II: partial solution), although still within the solution temperature range based on the thermal simulation and DSC results, the dissolution is slower as the temperature decreases. Unlike the PMZ, the short time of the welding thermal cycle does not seem to be sufficient for the complete
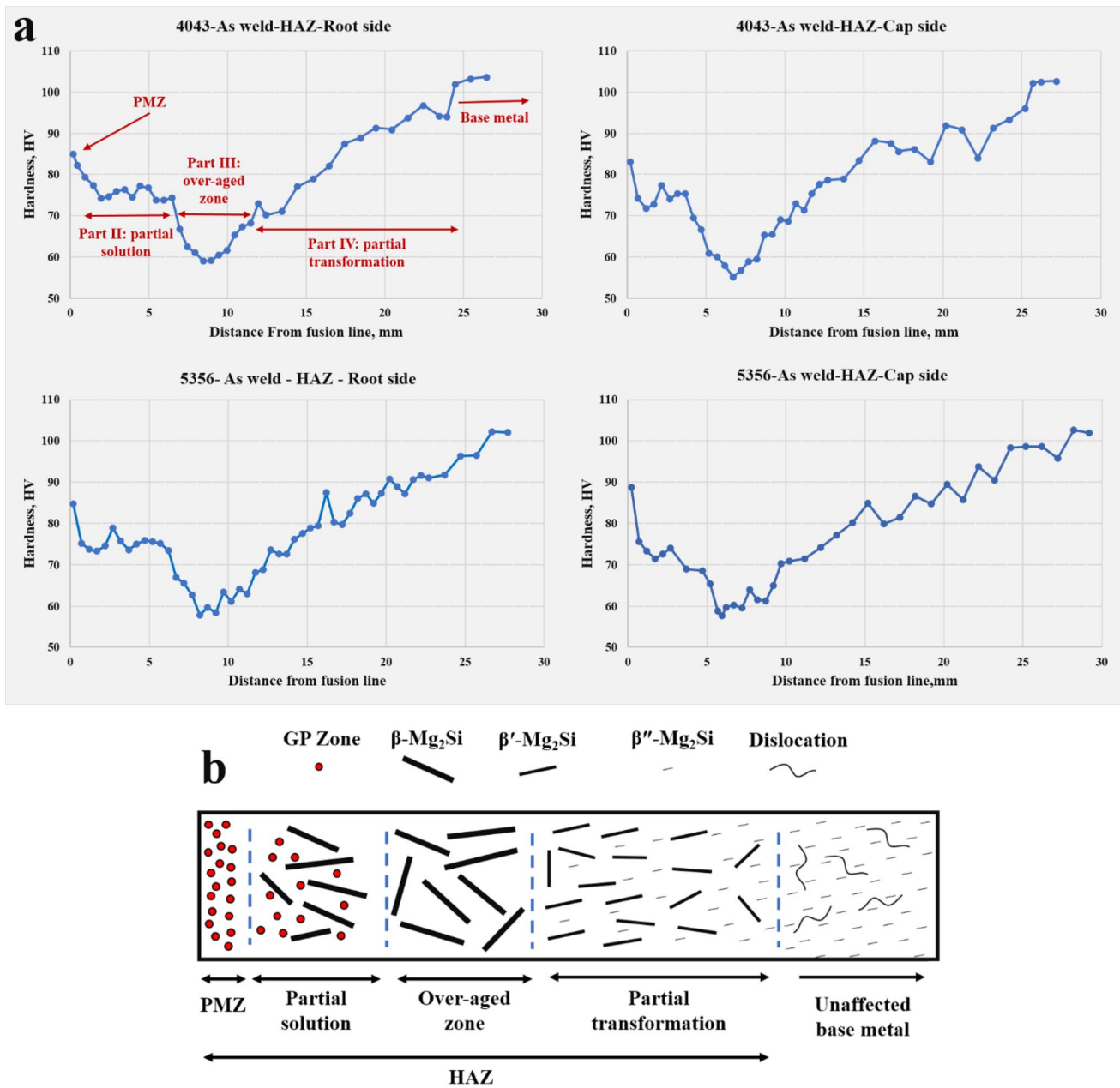
Fig. 7 Different parts of HAZ in the as-welded condition, **a** Microhardness profiles of the HAZ, **b** Schematic illustration of microstructure changes in different regions of the HAZ

dissolution of the Mg_2Si phases. Therefore, some Mg and Si are expected to dissolve in the matrix and contribute to forming a supersaturated solid solution and consequent natural aging. The remaining undissolved Mg and Si are transformed into the β-Mg_2Si. A higher transformation-to-dissolution ratio (greater distance from the fusion line and lower temperature) means less Mg and Si contribute to natural aging, resulting in lower hardness.

Parts of the HAZ farther from the fusion line are not within the solution annealing temperature range. Thus, the

initial β''-Mg_2Si phases are transformed according to the precipitation sequence described in the introduction. In the third part of the HAZ, the temperature is as high as the formation of β-Mg_2Si phases. Transformation of all Mg_2Si to the β-Mg_2Si phase causes the lowest hardness. As shown in Fig. 7, this region spatially corresponds to a significant valley approximately 7–9 mm from the fusion line in all the hardness profiles. The peak temperature of this area is about 300 °C or slightly higher (Fig. 8). This temperature is in the range of β' dissolution and subsequent β precipitation. TEM

a)

Peak temperature [°C]

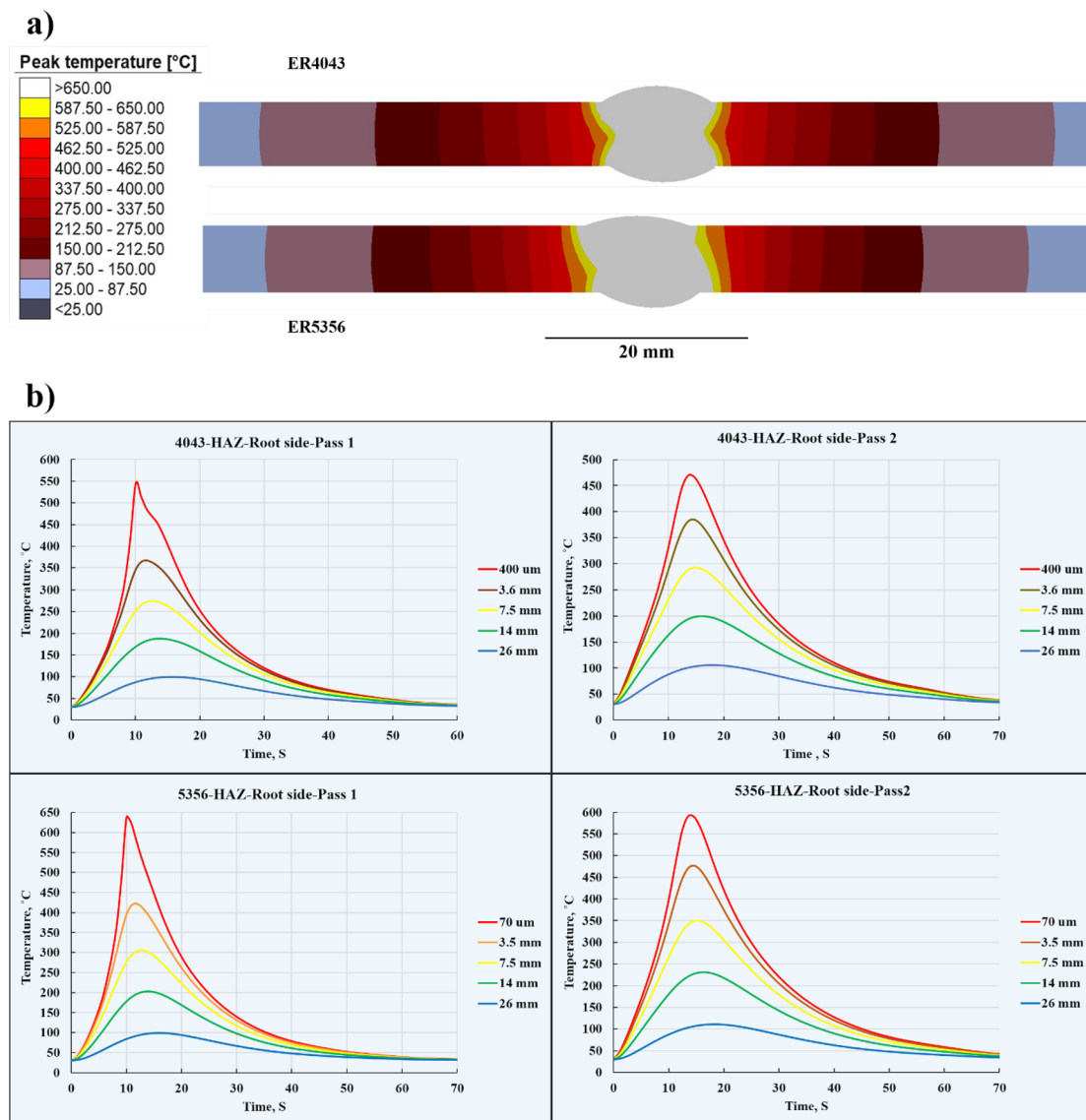|	
	>650.00
	587.50 - 650.00
	525.00 - 587.50
	462.50 - 525.00
	400.00 - 462.50
	337.50 - 400.00
	275.00 - 337.50
	212.50 - 275.00
	150.00 - 212.50
	87.50 - 150.00
	25.00 - 87.50
	<25.00

ER4043

ER5356

20 mm

b)

Fig. 8 Thermal simulation of the welding process, **a** Graphical illustration of thermal simulation results, **b** Time-Temperature curves of various points of HAZ

images were prepared to study the microstructure of the area with the lowest hardness and validate the analysis, which is presented in Fig. 10.

In the fourth part of HAZ (part IV: partial transformation), the temperature is within the β'-Mg$_2$Si phase formation range (180–280 °C according to peak a and b in Fig. 9) based on the precipitation sequence. Therefore, by transforming β''-Mg$_2$Si phases to β'-Mg$_2$Si, the hardness decreases somewhat, but it is higher than the hardness of the third part. With a further decrease in temperature, the transformation becomes slower and incomplete. Finally, it stops at a distance of about 25 mm from the fusion line, and the alloy is unaffected by welding thermal cycles.

Figure 8 shows the temperature below 100 °C in the unaffected area.

Considering Fig. 4a, it is clear that the observed dislocations in the base metal are not found in Fig. 10a. The heat of welding activates the recovery process and reduces dislocation density. As mentioned in 3.1, work hardening and subsequent increase in dislocation density were mechanisms for strengthening the base metal. Dislocation recovery is one of the reasons for reducing HAZ hardness. In addition, the coarsening of the Mg$_2$Si phases and their transformation to the β-Mg$_2$Si phase have also been identified. High-density spherical phases are still present in the microstructure and are not significantly different from the
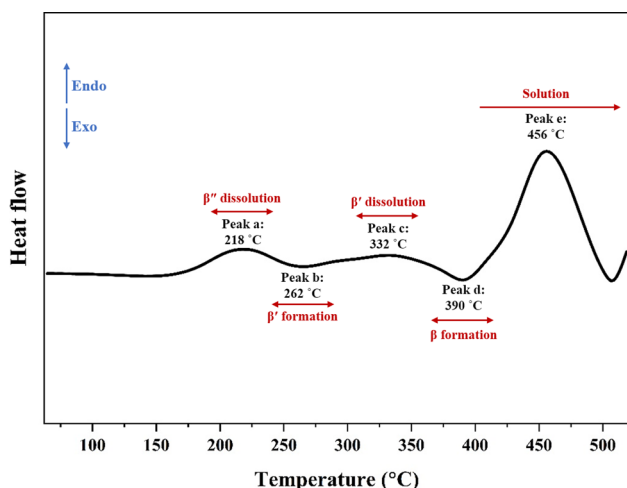
Fig. 9 DSC results of the as-received AA6082-T651 sample

base metal. Figure 10d presents the EDS analysis of the high-density spherical phase. It is a manganese-rich phase. The effect of the surrounding matrix on the EDS results is not ignorable due to the sub-micron dimensions of the studied phases. However, the richness of these phases in Mn can be deduced from the results. Microstructures, especially in Fig. 10c, demonstrate that some elongated coarse Mg_2Si phases have a higher density and appear dark in color. EDS analysis of referred precipitate, which is very large (β-Mg_2Si phase), shows that, in addition to being rich in Mg and Si, this phase also contains Cu. In fact, despite the low amount of copper in the chemical composition of the alloy (Table 1), it has entered the structure of Mg_2Si and made changes to it. Also, copper has increased the precipitate density.

3.3 Post-Weld Heat Treatment (PWHT)

This section investigates the microstructure and mechanical properties of HAZ after PWHT. Heat treatment consisted of solution annealing for 150 min at 530 °C and, following age hardening for 18 h at 160 °C. Based on DSC results (Fig. 9), the selected solution annealing temperature is sufficient to dissolve the Mg_2Si phases. Figure 11 represents the HAZ hardness profiles of heat-treated welds. A comparison of Figs. 7 and 11 reveals the elimination of the HAZ hardness trends after PWHT. Heat treatment has increased the hardness throughout the HAZ even more than the hardness of the base metal. The average microhardness results in Fig. 11 for ER4043 and ER5356 samples are 124.27 and 124.41, respectively. Furthermore, the variation of hardness from the mean for each indentation is less than 5%. Therefore, there is no significant change in the hardness results presented in Fig. 11, and the type of

filler metal does not affect the HAZ properties under PWHT conditions as well as under as-welded conditions.

The solution annealing has successfully dissolved the various phases formed in all parts of HAZ described in Sect. 3.2. Quenching the samples from 530 °C in water and immediately placing them in a furnace at 160 °C caused the highest driving force of age hardening. In other words, quench made a supersaturated solid solution of Mg and Si in the Al matrix. This thermodynamically unstable structure is the main driving force of aging. According to previous studies [51, 52], delay in aging and staying at ambient temperature causes the formation of GP zones and thus reduces driving force. In this work, minimizing the delay created the maximum driving force, which led to hardness in the range of 120 to 130 Vickers. The obtained hardness is not only higher than the hardness in as-welded conditions but also higher than that of the base metal. Therefore, the heat treatment cycle used in this work has successfully recovered the hardness throughout HAZ.

Figure 12 shows the TEM images of the microstructure of over-aged HAZ (part III) after PWHT. The results can accurately display the effect of PWHT on the sub-micron precipitates. Nano-sized precipitates are distinguishable from the Al matrix. Such phases are β″-Mg_2Si that grow in (100) crystallographic directions. Coarse over-aged β-Mg_2Si phases are no longer found in the microstructure. The microstructural changes demonstrate that the β-Mg_2Si was completely dissolved during solution annealing, and then β″-Mg_2Si was nucleated and grew from supersaturated solid solution during age hardening. The complete dissolution of over-aged phases, uniform distribution, and optimal size of precipitated β″-Mg_2Si was successfully achieved as microstructural aspects of the PWHT.

As mentioned in Sect. 3.1, the length and diameter of β″-Mg_2Si needles are reported up to 50 nm and about 4 nm, respectively [38, 39]. Accordingly, the phases observed in the TEM image (Fig. 12) were identified as β″-Mg_2Si based on their dimensions. The interface between β″-Mg_2Si and the Al matrix is coherent. Anderson et al. [53, 54] have reported that β″-Mg_2Si is coherent with the Al matrix along the b-axis of its monoclinic crystallographic structure, which is similar to the observations of this work. The lattice misfit of coherent precipitates and matrix induces an elastic strain field around the interface. The elastic strain field interacts with dislocations and impedes their movement. As a result, the yield strength and hardness are increased.

4 Conclusion

The HAZ of AA6082-T651 was investigated under as-welded and PWHT conditions. In the as-welded condition, significant softening of the HAZ was observed. An attempt
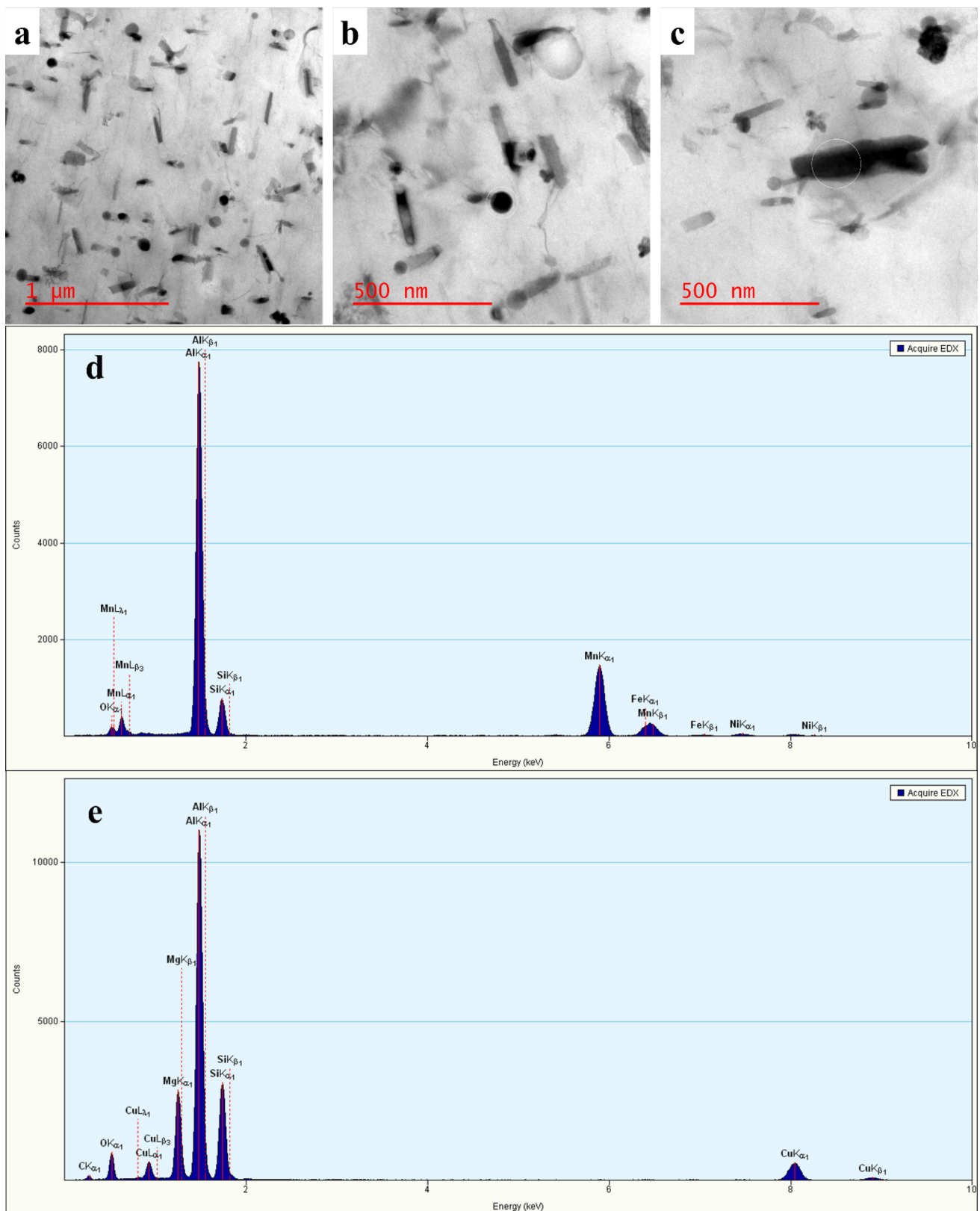
Fig. 10 TEM results of over-aged HAZ, which has the lowest hardness (TEM specimen was extracted from sample 1), **a** Bright field image of the microstructure, **b** of high-density spherical precipitate with higher magnification, **c** of coarse high-density elongated precipitate with higher magnification, **d** EDS analysis of indicated spherical phase, **e** of indicated elongated phase
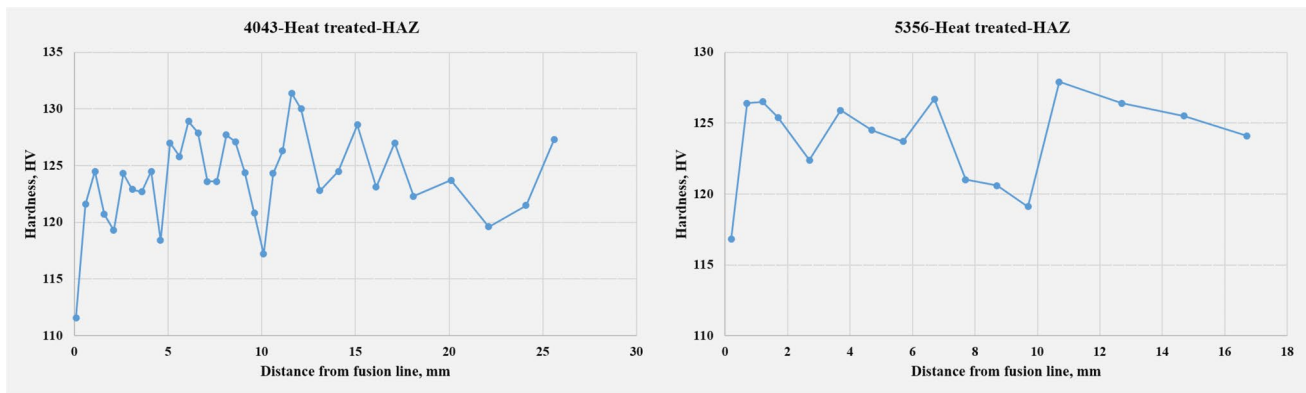
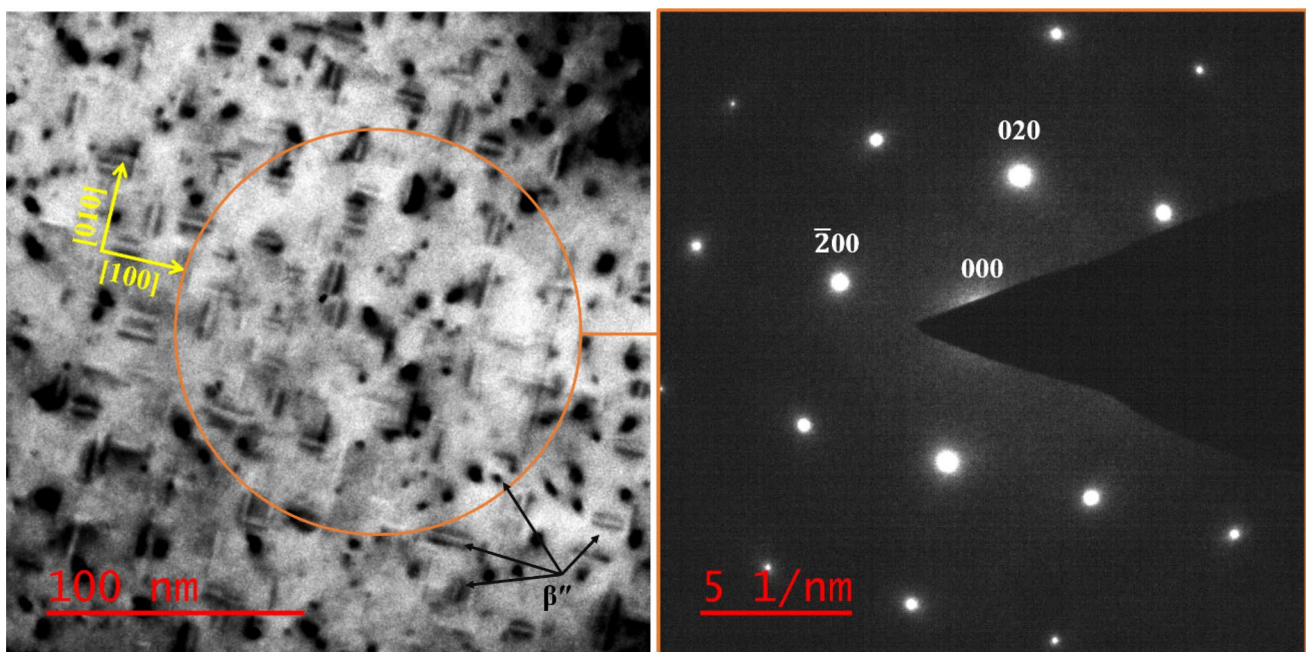**Fig. 11** The microhardness profiles of HAZ after PWHT

Fig. 12 Bright-field TEM image of over-aged region of HAZ (part III) after PWHT and corresponding SAD pattern (TEM specimen was extracted from sample 1)

was made to recover the softening by applying an appropriate PWHT. The main results are summarized as follows:

- The PWHT involved solution annealing at 530 °C for 150 min and 18 h of age hardening at 160 °C.
- The hardness of all HAZ parts was recovered and increased after PWHT and was even higher than the as-received base metal.
- TEM results of over-aged HAZ after PWHT revealed β″-Mg_2Si formation and complete elimination of the β-Mg_2Si.

- The hardness of as-received 6082-T651 was due to precipitation hardening and high dislocation density, which was identified through TEM results.
- A partially melted zone is identified adjacent to the fusion line. In this zone, the Mg_2Si phases were completely dissolved during welding, and then natural aging increased the hardness after welding.
- A distinctive valley is observed in HAZ microhardness profiles. It has the lowest HAZ hardness due to over aging of Mg_2Si phases and the formation of β-Mg_2Si.

References

1. E. George, D.S. Totten, Mackenzie, *Handbook of Aluminum: Vol. 1: Physical Metallurgy and Processes* (CRC Press, New York, 2003)
2. J.W. Bray, Aluminum mill and engineered wrought products, in *Properties and Selection: Nonferrous Alloys and Special-Purpose Materials*, vol. 2 (ASM International, Materials Park, 1990). https://doi.org/10.31399/asm.hb.v02.9781627081627
3. J.R. Kissell, R.L. Ferry, *Aluminum Structures: A Guide to Their Specifications and Design*, 2nd edn. (John Wiley & Sons, Hoboken, 2002)
4. N.H. Alharthi, Evaluation and prediction of microstructure evolution in deformed aluminum alloys, M.S. Thesis, Lehigh University (2011)
5. L. Zhang, R. Lu, J. Tang, F. Jiang, D. Fu, H. Zhang, J. Teng, Met. Mater. Int. (2022). https://doi.org/10.1007/s12540-022-01353-y
6. C. Vargel, *Corrosion of Aluminium*, 1st edn. (Elsevier, Amsterdam, 2004)
7. E.R. Imam Fauzi, M.S. Che Jamil, Z. Samad, P. Muangjunburee, J. Trans. Nonferrous Met. Soc. China. **27**, 17 (2017). https://doi.org/10.1016/S1003-6326(17)60003-7
8. A. Bandi, S.R. Bakshi, Met. Mater. Int. **28**, 1678 (2022). https://doi.org/10.1007/s12540-021-01039-x
9. S.R. Chikhale, K.P. Kolhe, A review on prediction of heat affected Zone of Al-6061 alloy. Int. J. Eng. Res. Special Issue, 54 (2015)
10. W.A. Monteiro, *Light Metal Alloys Applications*, 1st edn. (IntechOpen, Rijeka, 2014)
11. M. Hakem, S. Lebaili, S. Mathieu, D. Miroud, A. Lebaili, B. Cheniti, Int. J. Adv. Manuf. Technol. **102**, 2907 (2019). https://doi.org/10.1007/s00170-019-03401-1
12. EN 1999, Eurocode 9: Design of aluminium structures, European Standard (2007)
13. G. Mathers, *The Welding of Aluminium and Its Alloys* (Woodhead Publishing, Abington, 2002)
14. T. Anderson, *Welding Aluminum-Questions and Answers*, 2nd edn. (American Welding Society, Miami, 2010)
15. W. Ma, B. Wang, J. Lin, X. Tang, Trans. Nonferrous Met. Soc. China. **27**, 2454 (2017). https://doi.org/10.1016/S1003-6326(17)60272-3
16. N.E. Nanninga, High Cycle Fatigue of AA6082 and AA6063 Aluminum Extrusions, Ph.D. Thesis, Michigan Technological University (2008)
17. C.D. Marioara, S.J. Andersen, J. Jansen, H.W. Zandbergen, Acta Mater. **51**, 789 (2003). https://doi.org/10.1016/S1359-6454(02)00470-6
18. W. Chrominski, M. Lewandowska, Acta Mater. **103**, 547 (2016). https://doi.org/10.1016/j.actamat.2015.10.030
19. X. He, Q. Pan, H. Li, Z. Huang, S. Liu, K. Li, X. Li, Metals **9**, 173 (2019). https://doi.org/10.3390/met9020173
20. O.R. Myhr, Ã. Grong, H.G. Fjær, C.D. Marioara, Acta Mater. **52**, 4997 (2004). https://doi.org/10.1016/j.actamat.2004.07.002
21. S. Missori, A Sili, Mechanical behaviour of 6082-T6 aluminium alloy welds. Metall. Res. Technol. **18**(1), 12 (2000)
22. S. Baskutis, J. Baskutiene, R. Bendikiene, A. Ciuplys, J. Mech. Sci. Technol. **33**, 765 (2019). https://doi.org/10.1007/s12206-019-0131-6
23. W. Zhang, H. He, C. Xu, W. Yu, L. Li, JOM **71**, 2711 (2019). https://doi.org/10.1007/s11837-019-03375-1
24. B. Wang, S. Xue, C. Ma, J. Wang, Z. Lin, Metals **7**, 463 (2017). https://doi.org/10.3390/met7110463
25. P. Wiechmann, H. Panwitt, H. Heyer, M. Reich, M. Sander, O. Kessler, Materials **11**, 1396 (2018). https://doi.org/10.3390/ma11081396
26. ASTM E384-99, Standard Test Methods for Microindentation Hardness of Materials (ASTM International, West Conshohocken, 2002)
27. B. Wang, J. Wang, X. Liu, Q. Li, X. Liu, Mater. Sci. Eng. A **858**, 144090 (2022). https://doi.org/10.1016/j.msea.2022.144090
28. M.V. Kral, P.N.H. Nakashima, D.R.G. Mitchell, Metall. Mater. Trans. A **37**, 1987 (2006). https://doi.org/10.1007/s11661-006-0141-8
29. S. Ferraro, A. Fabrizi, G. Timelli, Mater. Chem. Phys. **153**, 168 (2015). https://doi.org/10.1016/j.matchemphys.2014.12.050
30. X.D. Ren, L. Ruan, S.Q. Yuan, N.F. Ren, L.M. Zheng, Q.B. Zhan, J.Z. Zhou, H.M. Yang, Y. Wang, F.Z. Dai, Mater. Sci. Eng. A **578**, 96 (2013). https://doi.org/10.1016/j.msea.2013.04.034
31. W.S. Lee, Z.C. Tang, Mater. Des. **58**, 116 (2014). https://doi.org/10.1016/j.matdes.2014.01.053
32. S.W. Nam, D.H. Lee, Met. Mater. **6**, 13 (2000). https://doi.org/10.1007/BF03026339
33. A.F.M. Muggerud, E.A. Mørtsell, Y. Li, R. Holmestad, Mater. Sci. Eng. A **567**, 21 (2013). https://doi.org/10.1016/j.msea.2013.01.004
34. X. Qian, N. Parson, X.G. Chen, Mater. Sci. Eng. A **764**, 138253 (2019). https://doi.org/10.1016/j.msea.2019.138253
35. A.M.F. Muggerud, Transmission electron microscopy studies of dispersoids and constituent phases in al-mn-fe-si alloys, Ph.D. Thesis, Norwegian University of Science and Technology (2014)
36. A.M.F. Muggerud, Y. Li, R. Holmestad, Acta Cryst. **70**, 888 (2014). https://doi.org/10.1107/S2052520614017880
37. Y.J. Li, A.M.F. Muggerud, A. Olsen, T. Furu, Acta Mater. **60**, 1004 (2012). https://doi.org/10.1016/j.actamat.2011.11.003
38. R. Vissers, M.A. van Huis, J. Jansen, H.W. Zandbergen, C.D. Marioara, S.J. Andersen, Acta Mater. **55**, 3815 (2007). https://doi.org/10.1016/j.actamat.2007.02.032
39. Z. Xu, H. Ma, N. Zhao, Z. Hu, Metals **10**, 469 (2020). https://doi.org/10.3390/met10040469
40. BS EN 485-2, Aluminum and Aluminum alloys - Sheet, Strip, and Plate. Part 2: Mechanical Properties, British Standard (2016)
41. J.M. Sánchez-Amaya, T. Delgado, L. González-Rovira, F.J. Botana, Appl. Surf. Sci. **255**, 9512 (2009). https://doi.org/10.1016/j.apsusc.2009.07.081
42. T.K. Chu, C.Y. Ho, in *Thermal Conductivity 15*, ed. by V.V. Mirkovich (Springer, Boston, 1978), p. 79
43. E. Kaschnitz, L. Kaschnitz, S. Heugenhauser, Int. J. Thermophys. **40**, 27 (2019). https://doi.org/10.1007/s10765-019-2490-8
44. I. Dutta, S.M. Allen, J. Mater. Sci. Lett. **10**, 323 (1991). https://doi.org/10.1007/BF00719697
45. W.F. Miao, D.E. Laughlin, Scr. Mater. **40**, 873 (1999). https://doi.org/10.1016/S1359-6462(99)00046-9
46. J. Osten, B. Milkereit, C. Schick, O. Kessler, Materials **8**, 2830 (2015). https://doi.org/10.3390/ma8052830
47. Z. Chen, K. Liu, E. Elgallad, F. Breton, X.G. Chen, Metals **10**, 763 (2020). https://doi.org/10.3390/met10060763
48. G. Asghar, L. Peng, P. Fu, L. Yuan, Y. Liu, Mater. Des. **186**, 108280 (2020). https://doi.org/10.1016/j.matdes.2019.108280
49. J. Schällibaum, T. Burbach, C. Münch, W. Weiler, A. Wahlen, Mater. Sci. Eng. Technol. **46**, 704 (2015). https://doi.org/10.1002/mawe.201500402
50. P.V. Witzendorff, S. Kaierle, O. Suttmann, L. Overmeyer, J. Mater. Process. Technol. **225**, 162 (2015). https://doi.org/10.1016/j.jmatprotec.2015.06.007

51. K. Strobel, M.A. Easton, L. Sweet, M.J. Couper, J.F. Nie, Mater. Trans. **52**, 914 (2011). https://doi.org/10.2320/matertrans.L-MZ201111
52. S. Esmaeili, D.J. Lloyd, Mater. Sci. Forum **519-521**, 169 (2006). https://doi.org/10.4028/www.scientific.net/MSF.519-521.169
53. H.W. Zandbergen, S.J. Andersen, J. Jansen, Science **277**, 1221 (1997). https://doi.org/10.1126/science.277.5330.1221
54. S.J. Anderson, H.W. Zandbergen, J. Jansen, C. TrÆholt, U. Tundal, O. Reiso, Acta Mater. **46**, 3283 (1998). https://doi.org/10.1016/S1359-6454(97)00493-X